University of Bath

High performance bifunctional electrocatalytic activity of a reduced graphene oxide - molybdenum oxide hybrid catalyst

Sundaram Chandrasekaran[a], Eui Jung Kim[a], Jin Suk Chung[a], Chris R Bowen[b], Balasubramaniyan Rajagopalan[a], Vaia Adamaki [b], R.D.K. Misra[c], and Seung Hyun Hur*[a]

The advances in cost effective, highly active and stable electrocatalysts for the oxygen reduction reaction (ORR) and the oxygen evolution reaction (OER) remain the major issues for the commercialization of metal air-batteries and alkaline fuel cells. In this aspect, a facile hydrothermal route was developed to prepare nonprecious metal electrocatalysts including pristine MoO_3 rods, nanospheres, and their hybrids with reduced graphene oxide (rGO). This is the first report of the use of rGO coupled with hexagonal MoO_3 nanocrystals to act as both ORR and OER catalysts. The rGO - MoO_3 sphere hybrid catalyst exhibited excellent catalytic activity toward both the ORR and OER than pristine MoO_3 rods, MoO_3 spheres and rGO- MoO_3 rods. In addition, the rGO - MoO_3 nanosphere hybrid exhibited excellent catalytic activity, long-term durability, and CO tolerance compared to a high quality commercial Pt/C catalyst. This makes the GMS hybrid composite a highly promising candidate for high-performance non-precious metal-based bi-functional electrocatalysts with low cost and high efficiency for electrochemical energy conversion. The enhanced activity of the rGO - MoO_3 nanosphere hybrid is due mainly to the enhanced structural openness in the tunnel structure of the hexagonal MoO_3 when it is coupled with rGO.

1. Introduction

The advancement of cost effective, naturally abundant, environmentally benign, and highly active catalysts for energy conversion and storage is of utmost importance and is an important topic in renewable energy research[1-4]. In particular, water splitting[5], fuel cells[6] and metal-air batteries[7] are required for future energy conversion and storage applications as a result of their high theoretical energy density. The oxygen reduction reaction (ORR) and oxygen evolution reaction (OER) play major roles in these devices. In this context, the discovery of robust materials for both the OER and ORR is important but also very challenging. Traditional catalysts, such as Pt and its alloys, perform well for the ORR, but their high cost limits their applications[8-11]. Materials such as, iridium and ruthenium-based compounds and their oxides are well known OER catalysts[12-14]. These metals are also expensive and among the rarest elements on earth, making them impractical for large-scale applications. Therefore, alternative catalysts based on cost effective, metal-free materials or non-precious metals have attracted considerable attention[4]. As a result, a number of non-precious nanomaterials, such as $Ni_{0.2}Co_{0.3}Ce_{0.5}O_x$[15], NiO_x-Bi[16] and Ni_3S_2[17], have been explored for their high OER activity. Recently, a range of uni-functional carbon materials or metal oxides with carbon materials also have been reported to exhibit high activities either for the OER or for ORR activity[18-23]. However, the use of single catalyst as a bi-functional catalyst[24-32] has rarely been reported because the bi-functionality requires significantly low over potentials and high activities for both the OER and ORR. Therefore, it remains a considerable challenge to design a high-performance catalyst capable of unifying the both OER and ORR for energy conversion and storage applications with the relevant properties of high activity, low-cost, carbon monoxide (CO) tolerance, and excellent stability.

Recently, a wide range of molybdenum oxide-based compounds with the manifold structural motifs and properties have attracted considerable interest in the field of materials research. These materials have been shown to exhibit excellent properties for catalysis[33, 34], photocatalysis[35], batteries[36], solar energy conversion[37, 38], and sensors[39, 40]. In crystallographic view, MoO_3 exists in three phases, orthorhombic α-MoO_3, monoclinic β-MoO_3, and hexagonal H-MoO_3. The hexagonal H-MoO_3 system is a metastable phase, which is constructed from the zigzag chains of octahedral [MoO_6] as the building blocks attached through adjacent oxygen. Compared to α and β crystal structures, hexagonal MoO_3 retains a number of interesting properties. The tunnel structure of H-MoO_3 can result in electron-hole separation and afford large special locations for cation insertion and extraction[41]. To date, there are no reports of multifunctional catalysts based on a hexagonal molybdenum oxide embedded graphene material for ORR and OER activity. Importantly the three essential factors to achieve in commercializing fuel technologies include high efficiency, stability, and scalability[42]. In this regard, the present study focused on a catalyst that is not only highly active but is also facile, robust, highly stable, and easily scalable. This paper reports the first, highly active

[a.] School of Chemical Engineering, University of Ulsan, Daehak-ro, 102, Nam-gu, Ulsan 680-749, South Korea.
[b.] Department of Mechanical Engineering, University of Bath, Bath, BA2, 7AY, U.K.
[c.] Department of Metallurgical, Materials and Biomedical Engineering, University of Texas at El Paso, TX, 79968-0521, USA.
*corresponding author: shhur@ulsan.ac.kr (Prof. S. H. Hur)

and multifunctional reduced graphene oxide (rGO) - hexagonal MoO_3 hybrid catalysts synthesized via a facile hydrothermal route. For sample identification, the prepared MoO_3 rods, MoO_3 nanospheres, rGO-MoO_3 rods, and rGO-MoO_3 nanosphere samples are denoted as MR, MS, GMR, and GMS respectively. The synthesized materials were tested for both the ORR and OER reactions and GMS hybrid shows promising performance compared to a high quality commercial Pt/C catalyst, indicating its potential as a cost effective and highly active bi-functional catalyst.

Experimental Section

2.1 Catalysts Synthesis

In a typical procedure of MR, 3 mmol of ammonium heptamolybdate tetrahydrate ((NH_4)$_6Mo_7O_2.4H_2O$) was dissolved in 50 mL of distilled water and 3 mmol HCl was then added to the reaction solution with vigorous stirring. The resulting solution was transferred to a 100 mL Teflon-lined stainless autoclave and sealed tightly, which was kept at 180 °C for 14 h. The autoclave was then allowed to cool naturally to room temperature. The resulting products were filtered, washed several times with absolute ethanol and distilled water, and dried at 250 °C for 4 h. The MS sample was synthesized using the same procedure, only the HCl was replaced with ammonia.

The graphene oxide (GO) was synthesized from graphite powders using a modified Hummers' method. In a typical synthesis of the GMR or GMS, 20 mg of MR or MS was added gradually to 20 mL of the GO solution. The mixture solution was then stirred magnetically, and 5 mL of ammonia was added gradually to the mixture. After 2 h, the resulting stable suspension was then transferred to a Teflon-lined autoclave, and treated hydrothermally at 180 °C for 14 h. Finally, the as-prepared product was dried at 250 °C for 4 h.

2.2 Instrumental analysis

The crystalline phases were identified by X-ray diffraction (XRD; Rigaku) using Cu-Kα radiation. The surface morphologies were identified by field emission scanning electron microscopy (FE-SEM; JSM 6500F) and transmission electron microscopy (TEM; JEOL JEM 2100F). The vibrational, rotational and other low-frequency modes in the sample were analyzed by Raman spectroscopy (Thermo Scientific DXR). The material composition and oxidation states of carbon and iron atoms in the GMS nanocomposites were analyzed by X-ray photoelectron spectroscopy (XPS, Thermo Scientific K-alpha). N_2 adsorption–desorption measurements were carried out at 77 K using a Micromeritics ASAP 2020 gas-sorption system. Thermogravimetric analysis (TGA) was carried out on Q50 (TA instruments) thermo-analyser under air atmosphere at a heating rate of 10 °C min^{-1}. The samples were heated from room temperature to 800 °C at a linear heating rate.

2.3 Electrochemical measurements

The electrochemical measurements were carried out in 0.1 M KOH at room temperature by cyclic voltammetry (CV, BioLogic, SP-50, USA) with a rotating disk electrode (RDE, 3 mm in diameter, RRDE-3A, ALS Co., Japan). The three-electrode cell consisted of an Ag/AgCl electrode as the reference electrode, Pt as the counter-electrode, and a glassy carbon electrode/rotating disk electrode (RDE) loaded with the various catalysts as the working electrode. As the working electrode, the electroactive materials in ethanol (1 mg/ml) and 10 µL of Nafion solution (0.5 wt% in isopropanol) as a binder were mixed by sonication. Subsequently, all the catalyst loading in the same amount of ~ 0.10 mg cm^{-2} was coated on a glassy-carbon RDE and dried in air for the electrochemical characterization. Finally, the measured potential vs. Ag/AgCl was converted to the reversible hydrogen electrode (RHE) scale using the Nernst equation.

3. Results and Discussion

The size, morphology, and hybrid structure of all samples were examined by scanning electron microscopy (SEM) and high resolution transmission electron microscopy (HR-TEM). **Fig. 1** shows the microscopic images of pristine MoO_3 rods (MR), rGO - MoO_3 rods (GMR), and pristine MoO_3 spheres (MS). **Fig. S1** represents FE-SEM images of pristine rGO used in the preparation of GMR and GMS hybrids. From the microscopic images **(Fig. 1(a-d))** of prepared MR sample, it evidently shows a unique rod-like morphology. The length of rods is about 8-12 µm and the average width is ~ 400-500 nm as shown in **Fig. 1(a-d)**. The fact demonstrated that, an addition of HCl in the reaction process was crucial for pure hexagonal-MoO_3 formation[43]. During the synthesis, acidic additives (HCl) turned out to be most effective in terms of rod formation and morphology control[44]. The H$^+$ concentration influences a rapid precipitation and resulted the formation of H-MoO_3. In other words, the H$^+$ is crucial to the formation of H-MoO_3 rod like structures[44-46]. **Fig. 1(e-h)** shows the microscopic images of rGO-MoO_3 (GMR) rods structures, where the average width of 100-125 nm of MoO_3 rods were hybrid with the rGO. Besides, it is to note that the nano spheres of MoO_3 (for MS sample) with the average diameter of ~10-20 nm were obtained with addition of ammonia in the reactant solvent medium during synthesis as shown in **Fig. 1(i-l).** Generally, the organic additives during the synthesis play a crucial role both in inducing the MoO_3 nuclei and directing the crystal growth[47, 48]. The effect of ammonium ions on the nucleation and growth is critical in controlling the morphology of the MoO_3 nanostructures, moreover the crystallization of the hexagonal phase with sphere shape takes place through the self-assembly of MoO_6 with the assistance of $NH_4^+$and H_2O[49-51]. Finally the purity and crystallinity of samples is improved by temperature effect. The rGO - MoO_3 nanospheres (GMS) have a diameter of **~ 1**0-20 nm and consist of numerous smaller spheres, forming a porous structure, as shown in **Fig. 2**, where large amounts of MoO_3 nanoparticles are decorated on rGO. The GMS, Pt/C, GMR, MR, and MS catalysts showed Brunauer-Emmett-Teller (BET) surface areas of 158.185, 133.415, 28.788, 6.817, and 6.415 m^2 g^{-1}, respectively, as shown in **Fig. 2f** and **Fig. S2**.
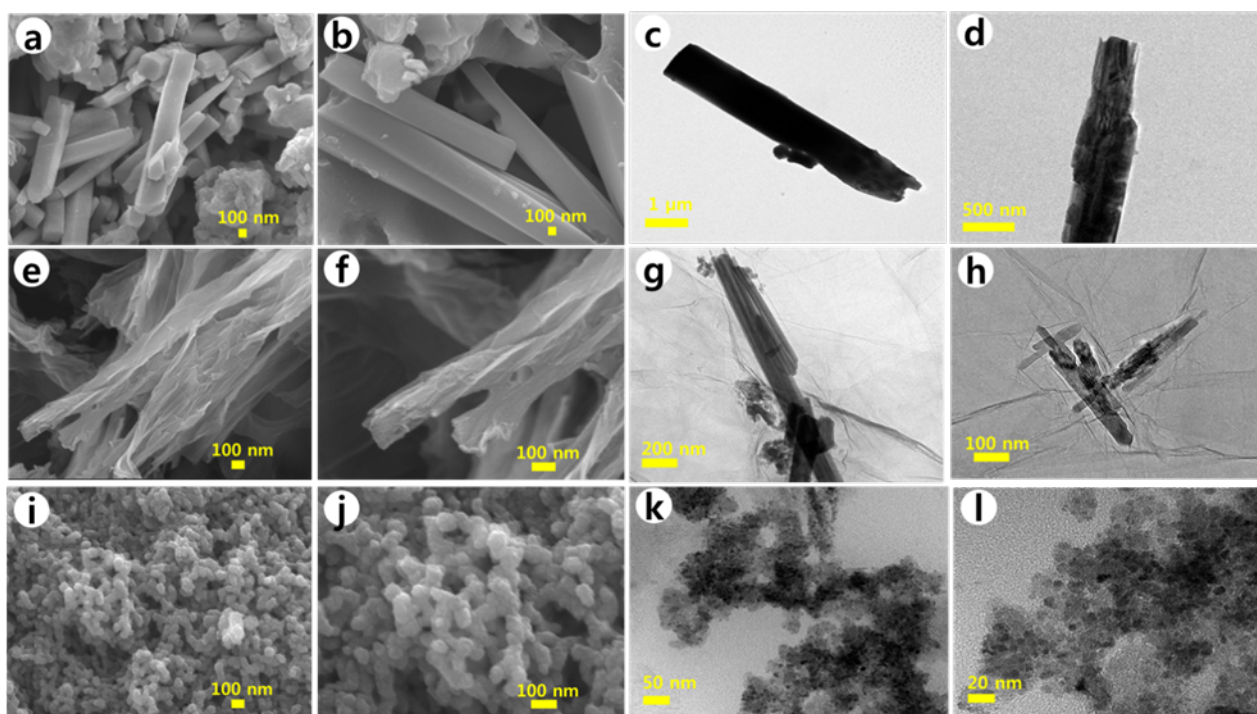
Journal Name

ARTICLE

Fig. 1 FE-SEM images (a,b); (e,f) and (i,j) of the MR, GMR, and MS samples, respectively; (c,d); (g,h) and (k,l) are TEM images of the MR, GMR, and MS samples, respectively.

The XRD patterns (**Fig. 3a**) show the good crystalline nature of all the prepared samples, as evidenced by the sharp XRD peaks, which can be indexed to the hexagonal MoO_3 phase JCPDS card (21-0569). In addition, the MR and GMR samples contained mixed phases of hexagonal MoO_3 and triclinic $Mo_{13}O_{33}$, which is in good agreement with the JCPDS card (21-0569 for H-MoO_3 and 82-1930 for $Mo_{13}O_{33}$). XRD indicated that for the GMR and GMS hybrids, the MoO_3 particles are purely formed on the graphene surface without the mixing of impurity particles. In the GMR and GMS hybrid structure, the presence of MoO_3 micro rods and nanoparticles reduces the aggregation of graphene sheets, which results in less stacking of the rGO sheets. As a result, a weak graphene related peak was observed in the XRD patterns.
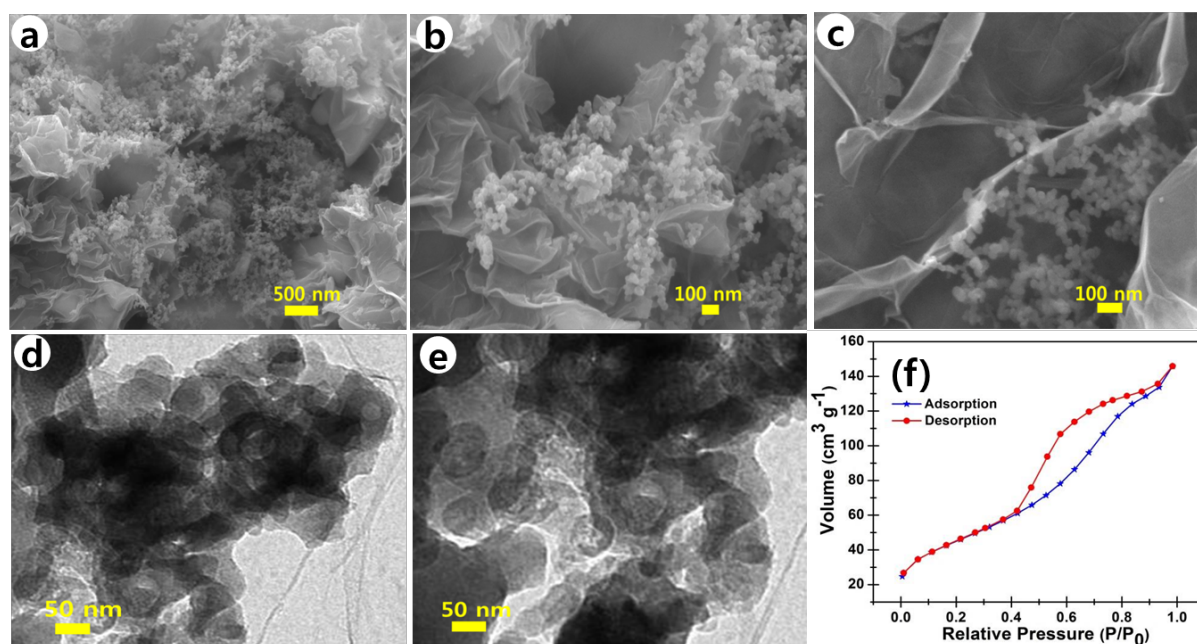
Fig. 2 FE-SEM images (a,b,c); (d,e) are TEM images and (f) represents the BET analysis of the GMS hybrid.
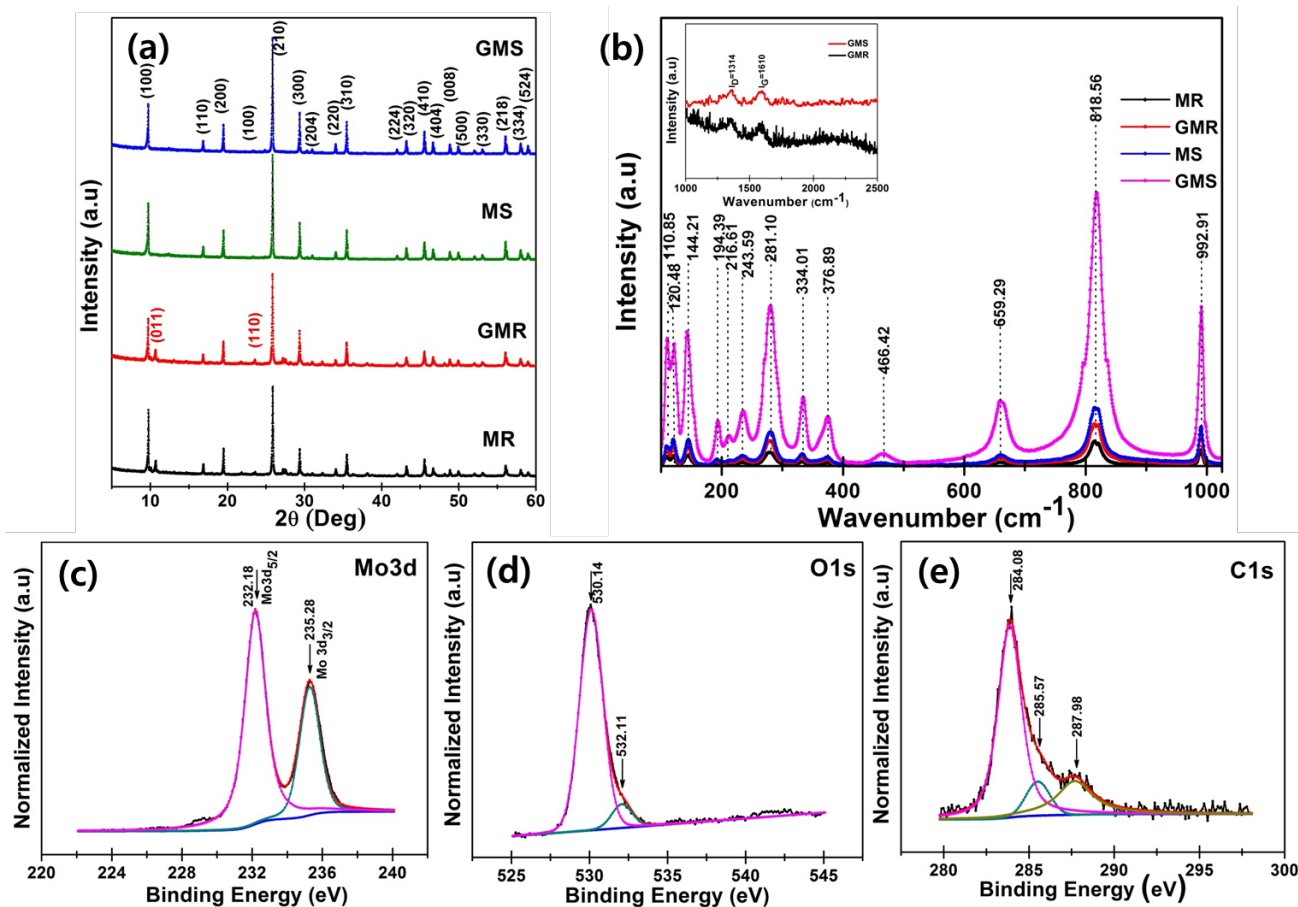

Fig. 3 (a) XRD patterns, (b) Raman spectra of MR, GMR, MS, and GMS hybrid (inserted graph represents the rGO peaks for the GMS and GMR samples); (c), (d) and (e) are XPS Mo3d, O1s and C1s core-level spectra of the GMS hybrid.

Fig. 3b shows the Raman spectra of the prepared pristine and graphene-MoO_3 nanocomposites of MR, MS, GMR and GMS. The intensity of the Raman peaks varies according to the crystal orientation and polarization of the laser source. The irreducible representation of MoO_3 with the space group D_{2h}^{16} (*Pbnm*) is known as follows: $\Gamma = 8A_g+8B_{1g}+4B_{2g}+4B_{3g}+4A_u+3B_{1u}+7B_{2u}+7B_{3u}$, where A_g, B_{1g}, B_{2g}, and B_{3g} are the Raman-active modes[40, 52]. A narrow band at ~ 993 cm^{-1} is the result of antisymmetric $vMo=O_1$ stretching (A_g), in which the bonding aligns along the *b* axis direction. Furthermore, the Raman peak at ~ 818 cm^{-1}, which is due to the stretching vibrations from the doubly coordinated bridging oxygen in the symmetric $vMo-O_3-Mo$ stretching (A_g) with the bonding along the a-axis, is the most intense Raman peak. The peak at 659 cm^{-1} and a weak peat at 466 cm^{-1} are fallouts of the asymmetric $vMo-O_2-Mo$ stretching (B_{2g}) and bending (A_g) modes, respectively[53]. The Raman peaks at 377 cm^{-1} were assigned to the B_{1g} mode due to the $\delta O_2=Mo=O_2$ scissor, and the 334 cm^{-1} peak is the characteristic of $\delta O_2=M=O_2$ deformation (B_{1g} mode). The broad band at 281 cm^{-1} corresponds to the wagging vibrations ($\delta O_1=Mo=O_1$ of B_{2g}

mode). The peaks at ~ 244, 217, 194 cm^{-1} can be attributed to the B_{3g}, A_g, and B_{2g} modes, respectively, due to the $\delta O_2=Mo=O_2$ scissor. The peaks at ~ 144, 120, and 111 cm^{-1} are the results from the deformation of MoO_3[54]. In addition, the peaks at ~ 1610 cm^{-1} and 1314 cm^{-1} correspond to the G and D bands of the graphene sheets for the GMR and GMS hybrids, respectively (inserted graph in **Fig. 3b**); the characteristic peaks of the MoO_3 particles and graphene appeared together in the GMR and GMS samples, suggesting the formation of the composites.

In addition, the electronic state and chemical composition of the GMS sample were examined by XPS. The XPS full scan survey spectra revealed the presence of Mo, C, and O in the rGO - MoO_3 nanocomposite, as shown in **Fig. S3a**. The **Fig. 3c-e** focuses on the XPS core level signatures at the rGO-MoO_3 interface, with the evolution of the Mo3d, O1s, and C1s core levels. The GMS hybrid sample features two main peaks at 232.18 eV and 235.28 eV, which are related to the Mo $3d_{3/2}$ and $3d_{5/2}$ components (**Fig. 3c**) with an integrated peak area ratio of 3:2 and a binding energy (ΔMo 3d = 3.1 eV), corresponding to an oxidation state of Mo(VI) for MoO_3, and

are indicative of a predominant Mo^{6+} oxidation state[40]. The O1s core-level spectrum of the GMS sample show two peaks at 530.14 eV and 532.11 eV corresponding to Mo-O and Mo-O-C bond formations, respectively, as shown in **Fig. 3d**. The C1s XPS spectra could be deconvoluted into three Gaussian peaks centered at 284.08, 285.57, and 287.98 eV, which were assigned to C-C/C=C, C-O, C=O, and O=C-O groups, respectively (**Fig. 3e**). The XPS data strongly support the XRD and Raman results and confirm the presence of MoO_3 on the surface of rGO in the GMS nanocomposite.

The chemical purity and thermal stability of MR, MS, GMR and GMS samples were evaluated by TGA under air atmosphere as shown in **Fig. S4**. When the samples heated from ambient temperature to 800° C, a prololonged decomposition starts at 200° C and extends upto 720° C leading to a total weight loss of 8.37, 9.27, 18.74 and 19.99 % for MR, MS, GMR and GMS samples respectively. Which indicates the highly stable nature of the prepared samples. These TGA results are in good agreement with previously reported results[55-59]. As shown in **Fig. S4**, MR and MS samples show a similar thermal decomposition trend under air conditions with a the nearby same weight loss of ~ 7 wt% up to 100-350° C, which was attributed to the removal of oxygen containing functional groups. Usually, the weight losses in the temperature range of 150° C - 300° C and 300° C - 600° C correspond to the removal of water and organic moiety respectively [51, 60]. For GMR and GMS nanocomposites, an obvious mass loss appeared between 230 and 600 °C, owing to the complete oxidation of graphene to carbon dioxide in air atmosphere. Then the curves showed thermal stability plateaus from 600, until 720 °C followed by an obvious mass loss due to melting and then evaporation of MoO_3 beyond 720 °C.

To assess the electrochemical oxygen reduction reaction (ORR) activity, the synthesized MR, MS, GMR, GMS catalysts and a high quality commercial Pt/C (HiSPEC™ 4000, Johnson Matthey, 53 wt% Pt) catalysts with the same loading were initially loaded onto glassy carbon electrodes to examine the cyclic voltammetry (CV) behavior in a 0.1 M KOH electrolyte saturated with either nitrogen (N_2) or oxygen (O_2) at a potential scan rate of 10 mV S^{-1} using a three-electrode system until reproducible CVs were obtained. Compared to the featureless CV profile in the N_2-saturated electrolyte (dotted red line in **Fig. 4a**), a strong reduction current peak was observed when the electrolyte was saturated with O_2 (solid black line in **Fig. 4a**), indicating the electrocatalytic activity of the as-synthesized samples toward oxygen cathodic reduction. The rotating disk electrode (RDE) technique was carried out to further investigate the electrocatalytic ORR behavior of all the synthesized catalysts and high purity commercial Pt/C samples.
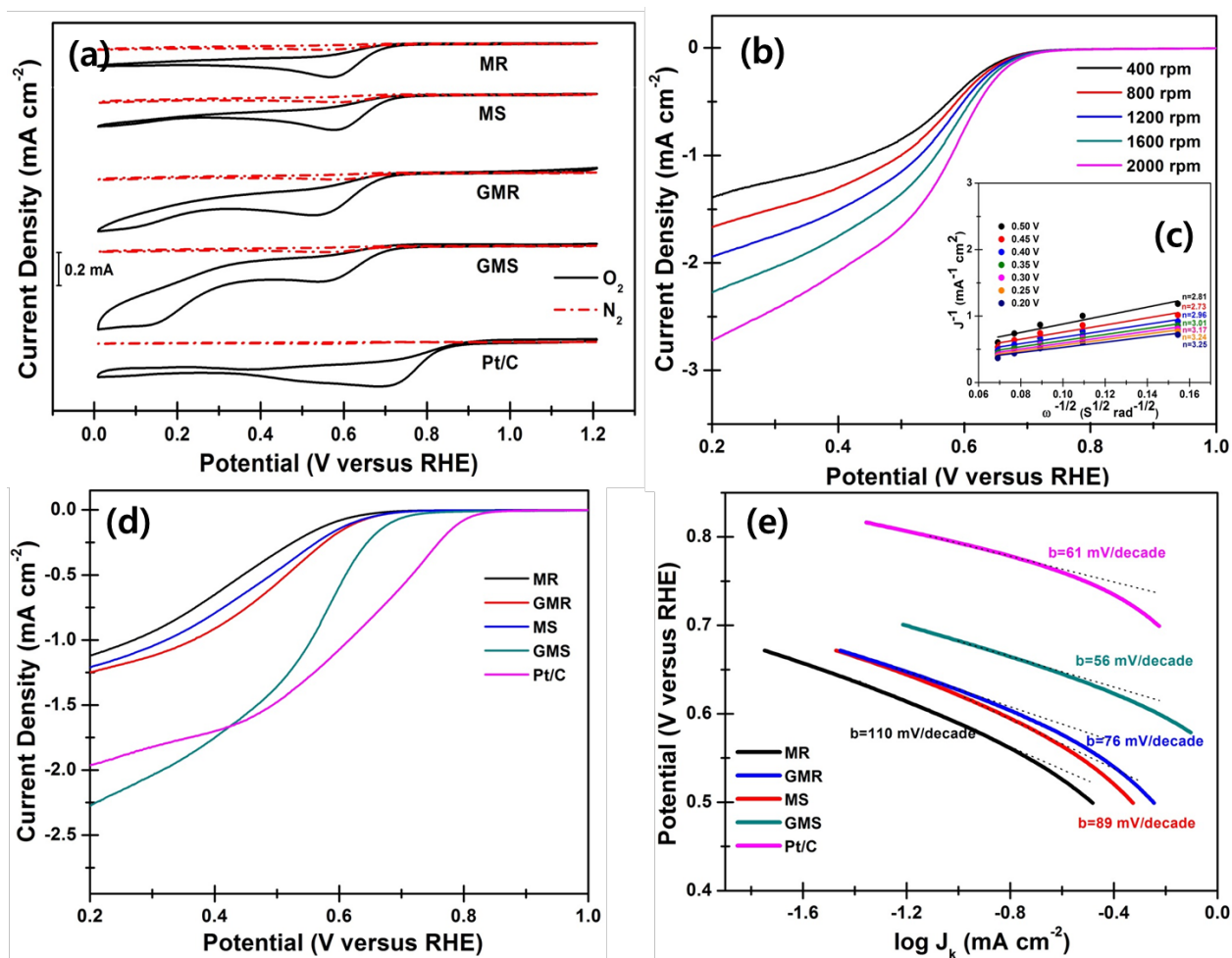
Fig. 4 (a) CV curves of MR, GMR, MS, and GMS hybrid in an O_2-saturated (solid black line) or N_2-saturated (dotted red line) 0.1 M KOH. (b) Rotating-disk voltammograms of the GMS hybrid in an O_2-saturated 0.1 M KOH with a sweep rate of 10 mV s^{-1} at various rotation speeds. The insets in (b) show corresponding Koutecky-Levich plots (J^{-1} versus $\omega^{-0.5}$) at different potentials. (c) ORR polarization curves of the MR, GMR, MS, GMS, and high quality commercial Pt/C catalysts in an O_2-saturated 0.1 M KOH at room temperature with a sweep rate of 10 mV s^{-1} at a rotation speed of 1600 rpm. (e) Tafel plots of all the samples including commercial Pt/C derived by a mass-transport correction of the corresponding RDE data.

The polarization curves were obtained by scanning the potentials at a scan rate of 10 mV s^{-1} at different rotation rates, as shown in **Fig. S5** for MR, MS and GMR catalysts, and in **Fig. 4b** for GMR catalyst. The linearity of the Koutecky-Levich plots and the near parallelism of the fitting lines (**Fig. S5** and inset of **Fig. 4c**) suggest first-order reaction kinetics toward the concentration of dissolved oxygen and similar electron transfer numbers for the ORR at different potentials.

Fig. 4d compares the polarization curves of MR, GMR, MS, GMS, and high quality Pt/C catalyst in an O_2-saturated 0.1 M KOH at room temperature with rotation at 1600 rpm. Remarkably, the ORR onset potential was 0.819 V vs. RHE for the GMS hybrid, and more positive than that of MR (0.738), MS (0.762 V), and GMR (0.767 V) catalyst as shown in **Fig. S6a**. Significantly, the MR, GMR, MS, and GMS catalysts, exhibited ORR activity with an electron transfer number of 3.1, 2.91, 3.2, and 3.3 at 0.2 V vs. RHE, respectively as shown in **Fig. S4** and **Fig. 4c**, suggesting a dominant reduction process. Compared to the prepared samples, the GMS hybrid structure showed enhanced ORR activity (**Fig. 4d**) because the addition of graphene, small sized particles, morphology, and exposed active faces have significant impacts on the catalytic activity in the GMS hybrid. In addition, the enhanced activity of the GMS hybrid is due to the higher structure openness in the tunnel structure of hexagonal MoO_3, which was not only coupled with graphene, but also provide an effective highway for the transportation of charges for an active catalytic activity[41]. This could provide more active sites in the GMS hybrid. Similarly, graphene prevents the agglomeration of MoO_3 nanospheres, which can also enhance the electrochemical performance. Moreover, the GMR and GMS hybrids afforded an ORR current density of 1.26 mA cm^{-2} and 2.27 mA cm^{-2}, respectively (**Fig. 4d**). The performance of the GMS hybrid catalyst was enhanced greatly compared to other catalysts. In addition, the diffusion-limiting current of the GMS nanocomposite was close to that of a commercial Pt/C catalyst (onset potential ~ 0.915 V) and the half-wave potential was ~ 114 mV lower than that of Pt/C.

On the other hand, the GMS hybrid catalyst has a higher current density (2.27 mA cm^{-2}) that that obtained using the commercial Pt/C catalyst (1.98 mA cm^{-2}) see **Fig. 4d**, which can be due to the higher electron accepting capability of the ORR active sites and the large surface area of the GMS hybrid. The excellent ORR activity of the GMS hybrid catalyst was also observed from the much smaller Tafel slope of 56 mV/decade at low over-potentials **(Fig. 4e)** than those measured with MR (110 mV/decade), GMR (76 mV/decade), MS (89 mV/decade), and high quality commercial Pt/C (61 mV/decade) in the O_2 saturated 0.1 M KOH electrolyte.

During durability testing (**Fig. 5a**), the GMS hybrid exhibited superior long term durability compared to the Pt/C catalyst in O_2 saturated 0.1 M KOH with less decay ($\triangledown$15% -

29%) of the ORR activity than that of the Pt/C catalyst ($\triangledown$35% - 48%) over 10,000 - 20,000 s of continuous operation with a rotation of 1600 rpm at 0.65 V vs. RHE (**Fig. 5a**). Although the GMR showed slightly higher activity, it suffered a 39% decrease in current density over 20,000 s of continuous operation in O_2 saturated 0.1 M KOH. In particular, in alkaline electrolytes (for alkaline fuel cells), the Pt catalyst degrades gradually over time due to surface oxides, aggregation, and particle dissolution. Long term durability is one of the most important properties for potential ORR active catalysts as electrocatalysts since they must operate for a long time in a harsh environment[61]. In this regard, the durability of GMR, GMS, and high quality commercial Pt/C was tested again using a glassy carbon electrode by continuously performing the ORR at 0.65 V vs. RHE in an O_2 saturated 0.1 M KOH solution. The results were compared with those obtained for commercial Pt/C catalyst under the same environment, as shown in **Fig. 6b**. These results suggest that the GMS hybrid structure has a larger long term durability than GMR and high quality commercial Pt/C catalysts.

In previous reports, the long-term stability of other ORR catalysts, such as Ag, Au, Pd, and bi-metallic nanocrystals, in alkaline solutions are improved relative to Pt, but they still suffer from deactivation and are below the targets for energy storage device applications[42, 61]. Poor catalyst durability is one of the major challenges for alkaline fuel cells. Hence, the excellent stability of this GMS hybrid makes it favorable for the ORR and further important catalytic kinetic reactions in alkaline solutions.

Typically, carbon monoxide (CO) molecules are one of the main poisons of fuel cell catalysts because of their strong coordination to active metal surfaces, which reduces the rate of the catalytic reaction. Importantly, the present hybrid exhibits superior CO tolerance to Pt/C catalyst due to the injection of a 3.0 M methanol solution in the middle of the RDE at a rotation of 1600 rpm. As shown in **Fig. 5c**, a rapid decrease in the normalized current was observed for the Pt/C catalyst immediately after the methanol injection. In contrast, there was almost no change in the GMS and GMR catalyst, which indicates the excellent CO tolerance of the graphene-MoO_3 hybrids fabricated in this study. The more positive ORR onset potential, the more positive half-wave potential, and the smaller Tafel slope measured by CV, RDE, long term durability, and CO tolerance indicates the excellent electrocatalytic performance of the GMS hybrid structures fabricated in this study. The enhanced ORR activity of the GMS hybrid may result from the small particle size, high surface area, higher structure openness in the tunnel structure of hexagonal MoO_3, and the thermal reduction of GO during the synthesis process. This is a result of the higher electrical conductivity of the rGO,

which can lead to better ORR activity of the resulting nanocomposites due to the effective charge transfer from MoO_3 to rGO[25, 30, 62].

To examine the OER electrocatalytic activity, CV and linear sweep voltammetry (LSV) were performed with the same catalysts loaded on the glassy carbon electrodes and a rotating disk electrode in an N_2-saturated 0.1 M KOH. For a direct comparison, the CV curves of the GMS hybrid, GMR, MR, and MS were measured to investigate their catalytic activity for the OER under the same conditions, as shown in **Fig. S3b**. From this CV curves, it shows that GMS has the lowest onset potential compared to the other catalysts. Further, to examine
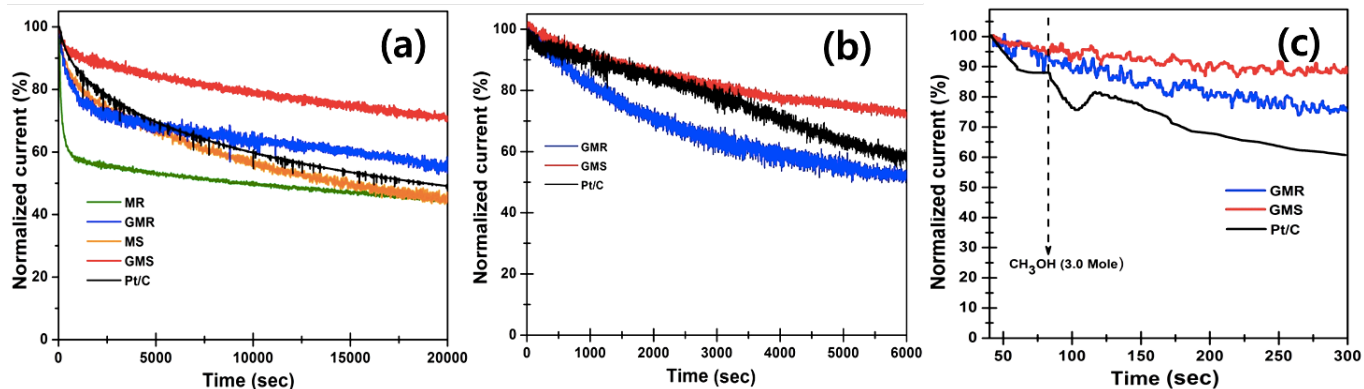

Fig. 5 Durability test by the chronoamperometric responses (percentage of current retained versus operation time/I–t test) of the MR, GMR, MS, GMS, and high-quality commercial Pt/C catalysts kept at 0.65 V versus RHE in an O2-saturated 0.1 M KOH electrolyte (a) at 1600 rpm and (b) Chronoamperometric responses of GMR, GMS, and a high-quality commercial Pt/C catalysts on glassy carbon kept at 0.65 V vs. RHE. (c) RDE measurements at 1600 rpm on the CO tolerance effect.
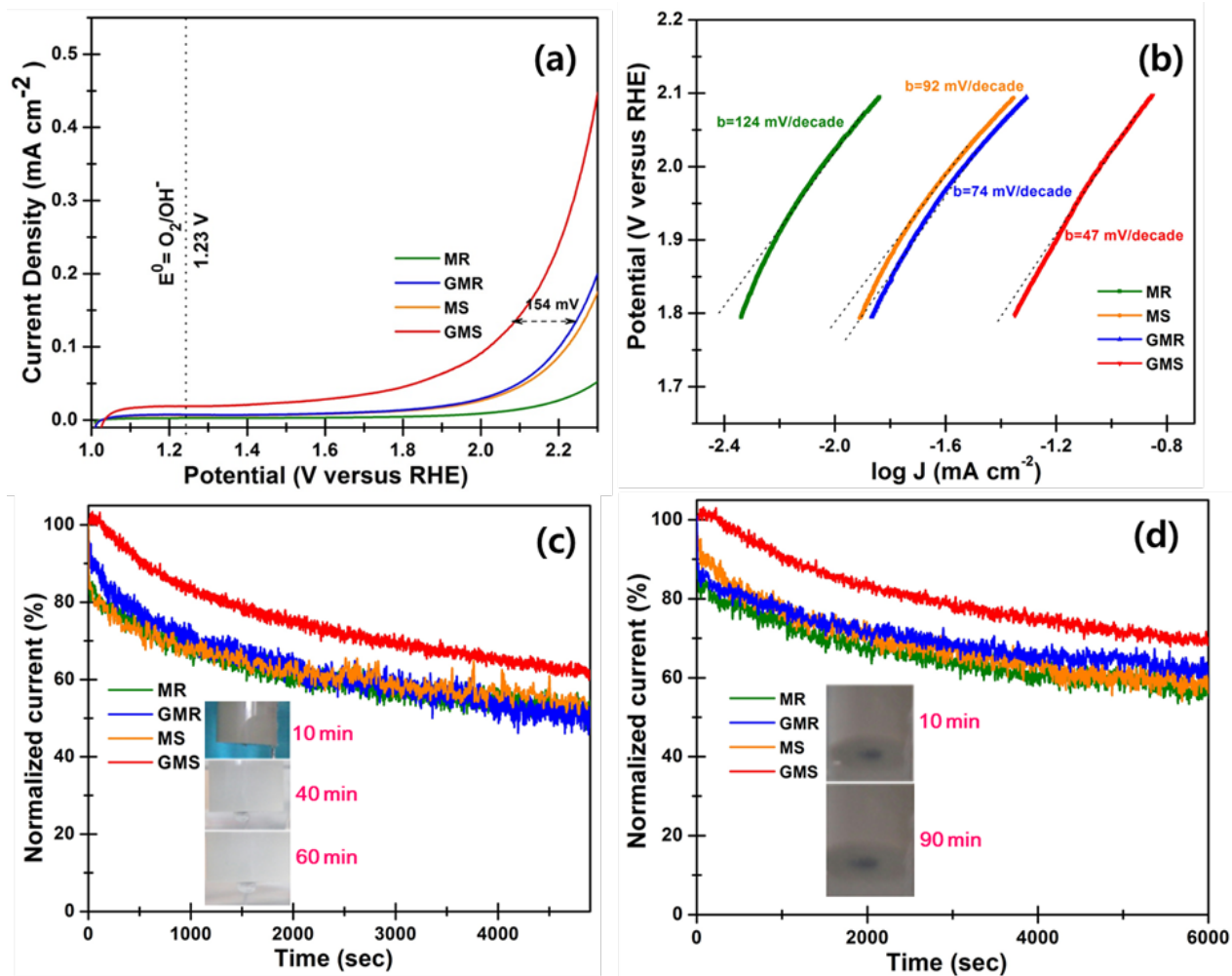
Fig. 6 (a) Oxygen evolution currents of MR, GMR, MS, and GMS hybrid measured in an N_2-saturated 0.1 M KOH with a sweep rate of 10 mV s^{-1}. (b) Tafel plots of the OER currents in (a). Durability test by the chronoamperometric responses (percentage of current retained versus operation time/I–t test) of the MR, GMR, MS, and GMS catalysts kept at 1.55 V versus RHE in a 0.1 M KOH electrolyte with a sweep rate of 10 mV s^{-1} in (c) glassy carbon electrode and the digital images in (c) show the gradual accumulation of evolved O_2 bubbles on the glassy carbon electrode at 10, 40, and 60 minutes during the I-t test. (d) RDE (with rotation of 1600 rpm) and the digital images in (d) show that there was no O_2 bubble accumulation on the rotating disk electrode at 10 (initial) and 90 (final) minutes during the I–t test.

the onset of the electrocatalytic OER, the LSVs of the catalysts were performed at a sweep rate of 10 mV s^{-1}, as shown in **Fig. 6a**. As shown in **Fig. 6a** the LSV curves, a small (~ 20 micro amp per cm^2) catalytic current was observed at approximately 1.23 V vs. RHE (standard potential for water splitting/OER) for the GMS. In the anodic scan, the GMS electrode exhibited a lower OER onset potential and higher OER peak current (0.12 mA cm^{-2} at an over potential of ~ 0.54 V as shown in **Fig. 6a**) than those of the other synthesized catalysts. The small Tafel slope was as low as 47 mV/decade, which is comparable to the best performance ever reported using other OER catalysts, as shown in **Fig. 6b** and **Table S1**. As an efficient oxygen evolution anode, GMS showed an onset potential of 1.768 V, which is much smaller than those of MR (~ 2.095 V), MS (~ 1.923 V), and GMR (~ 1.901 V), as shown in **Fig. S6b**.

On the glassy carbon electrode, the GMS catalyst suffered a huge current drop in the durability test (**Fig. 6c**); the GMS catalyst lost as much as ~38% of its activity after 5000 s operation. The rapid decay in current is mainly due to the obstruction of some active sites on the catalyst by the gradual accumulation of evolved oxygen (O_2) bubbles, as evidenced by the digital images of the electrode taken at 10, 40, and 60 minutes during the test, which clearly show that O_2 bubbles accumulated gradually on the catalyst surface. Consequently, all catalysts exhibited pronounced current decay, which could be caused by the accumulation of gas bubbles that partially block the active sites of the electrode. The other reason for the activity drop is that bubble formation on the catalyst surface may lead to peel-off and delamination of the catalyst from the electrode.

To avoid bubble formation on the electrodes, a durability test was performed using the RDE with a high rotation speed (1600 rpm). The RDE durability test results (**Fig. 6d**) also confirm that the long term stability of the catalyst is improved greatly (only ~ 26% activity loss after 6000 s operation) on the RDE and the digital images show that there was almost no O_2 bubble accumulation on the electrode. This is due to the evolved O_2 bubbles being removed from the catalyst and maintains a clean catalyst surface, thereby providing a more reliable way to examine the stability of the OER catalysts. These results make this GMS hybrid material the foremost bi-functional catalyst for both oxygen reduction and evolution. The strong interaction between the Mo oxide species and graphene/rGO during the formation of rGO-MoO_3 is crucial for improving the OER activity[63]. The present GMS catalyst outperformed previously reported catalysts with smaller over-potentials for both ORR and OER, indicating that it is one of the highest performance non-precious metal-based bi- functional catalysts; **Table S1** provides a detailed comparison. The excellent

catalytic activities of the GMS nanocomposite for both the ORR and OER may be attributed to three main factors. The first is the well-dispersed rGO/MoO_3 nanospheres with a heterogeneous nanocomposite structure (**Fig. 2**). The second is the high specific surface area of the nanocomposite, which can provide more active sites for both ORR and OER catalysis[64-67]. Thirdly, the formation of a tunnel structure of MoO_3 results in effective electron-hole separation and affords large special locations for cation insertion and extraction.

4. Conclusions

A facile hydrothermal route has been developed to prepare pristine MoO_3 rods, nanospheres, and their hybrids with reduced graphene oxide. While the MoO_3 rods and MoO_3 spheres alone have lower catalytic activity for the Oxygen Reduction Reaction (ORR) and Oxygen Evolution Reaction (ORR), their graphene hybrid materials exhibit, surprisingly high ORR activities in alkaline solutions, which are comparable to high quality commercial Pt/C catalysts and exceed the performance of Pt/C in terms of stability, durability, and CO tolerance. Graphene coupled with MoO_3 enables the complete use of the catalyst surface area by minimizing the agglomeration/restacking of graphene sheets, which greatly reduces the accessible surface area of the catalyst. In addition, the enhanced activity of the GMS hybrid can be attributed to the higher structural openness in the tunnel structure of hexagonal MoO_3 when it is coupled with rGO. This work presents a highly promising catalyst for alkaline fuel cells for which there has been a recent resurgence in interest as a solution to electrolyte carbonation. More importantly, the low cost of the synthetic method combined with their promising bifunctional catalytic activity, stability, durability, and CO tolerance effect makes graphene-MoO_3 a new class of electrocatalyst for the next generation fuel cells (both ORR and water splitting/OER). The GMS catalyst offers new opportunities for the development of ORR and OER catalysts with carbon and non-precious metal-based materials, and is believed to be a promising candidate for advanced catalysts for energy conversion.

Acknowledgements

Notes and references

‡ Footnotes relating to the main text should appear here. These might include comments relevant to but not central to the

matter under discussion, limited experimental and spectral data, and crystallographic data.

References

1. A. S. Arico, P. Bruce, B. Scrosati, J.-M. Tarascon and W. Van Schalkwijk, *Nat. Mater.*, 2005, **4**, 366.
2. J. S. Lee, S. Tai Kim, R. Cao, N. S. Choi, M. Liu, K. T. Lee and J. Cho, *Adv. Energy. Mater.*, 2011, **1**, 34.
3. B. Dunn, H. Kamath and J.-M. Tarascon, *Science.*, 2011, **334**, 928.
4. R. Bashyam and P. Zelenay, *Nature.*, 2006, **443**, 63.
5. A. Kudo and Y. Miseki, *Chem. Soc. Rev.*, 2009, **38**, 253.
6. Z. Zhang, J. Liu, J. Gu, L. Su and L. Cheng, *Energy Environ. Sci.*, 2014, **7**, 2535.
7. F. Cheng and J. Chen, *Chem. Soc. Rev.*, 2012, **41**, 2172.
8. J. Wu and H. Yang, *Acc. Chem. Res.*, 2013, **46**, 1848.
9. J. Zhang, K. Sasaki, E. Sutter and R. Adzic, *Science.*, 2007, **315**, 220.
10. J. Zhang, M. B. Vukmirovic, Y. Xu, M. Mavrikakis and R. R. Adzic, *Angew. Chem. Int. Ed.*, 2005, **44**, 2132.
11. G. Zhang, S. Sun, M. Cai, Y. Zhang, R. Li and X. Sun, *Sci. Rep.*, 2013, **3**, 1526 .
12. G. Zehl, G. Schmithals, A. Hoell, S. Haas, C. Hartnig, I. Dorbandt, P. Bogdanoff and S. Fiechter, *Angew. Chem. Int. Ed.*, 2007, **46**, 7311.
13. H.-G. Jung, Y. S. Jeong, J.-B. Park, Y.-K. Sun, B. Scrosati and Y. J. Lee, *ACS Nano*, 2013, **7**, 3532.
14. H. G. Sanchez Casalongue, M. L. Ng, S. Kaya, D. Friebel, H. Ogasawara and A. Nilsson, *Angew. Chem. Int. Ed.*, 2014, **53**, 7169.
15. J. A. Haber, Y. Cai, S. Jung, C. Xiang, S. Mitrovic, J. Jin, A. T. Bell and J. M. Gregoire, *Energy Environ. Sci.*, 2014, **7**, 682.
16. C. Xiao, X. Lu and C. Zhao, *Chem. Commun.*, 2014, **50**, 10122.
17. W. Zhou, X.-J. Wu, X. Cao, X. Huang, C. Tan, J. Tian, H. Liu, J. Wang and H. Zhang, *Energy Environ. Sci.*, 2013, **6**, 2921.
18. H. Wang, Y. Liang, Y. Li and H. Dai, *Angew. Chem. Int. Ed.*, 2011, **50**, 10969.
19. M. Zhang and L. Dai, *Nano Energy*, 2012, **1**, 514.
20. S. Chen, J. Duan, M. Jaroniec and S. Z. Qiao, *Angew. Chem. Int. Ed.*, 2013, **52**, 13567.
21. X. Long, J. Li, S. Xiao, K. Yan, Z. Wang, H. Chen and S. Yang, *Angew. Chem. Int. Ed.*, 2014, **126**, 7714.
22. J. Suntivich, K. J. May, H. A. Gasteiger, J. B. Goodenough and Y. Shao-Horn, *Science*, 2011, **334**, 1383.
23. F. Song and X. Hu, *Nat. Commun.*, 2014, **5**, 5477.
24. Y. Meng, W. Song, H. Huang, Z. Ren, S.-Y. Chen and S. L. Suib, *J. Am. Chem. Soc.*, 2014, **136**, 11452.
25. Y. Liang, Y. Li, H. Wang, J. Zhou, J. Wang, T. Regier and H. Dai, *Nat. Mater.*, 2011, **10**, 780.
26. S. Mao, Z. Wen, T. Huang, Y. Hou and J. Chen, *Energy Environ. Sci.*, 2014, **7**, 609.
27. Q. Liu, J. Jin and J. Zhang, *ACS Appl. Mater. Interfaces.*, 2013, **5**, 5002.
28. D. Wang, X. Chen, D. G. Evans and W. Yang, *Nanoscale*, 2013, **5**, 5312.
29. Y. Gorlin and T. F. Jaramillo, *J. Am. Chem. Soc.*, 2010, **132**, 13612.
30. Y. Liang, Y. Li, H. Wang and H. Dai, *J. Am. Chem. Soc.*, 2013, **135**, 2013.
31. W. Zhou and J. Sunarso, *J. Phys. Chem. Lett.*, 2013, **4**, 2982.
32. M. Jahan, Z. Liu and K. P. Loh, *Adv. Funct. Mater.*, 2013, **23**, 5363.
33. J. Tatibouet and J. Germain, *J. Catal.*, 1981, **72**, 375.
34. H. Cheng, T. Kamegawa, K. Mori and H. Yamashita, *Angew. Chem. Int. Ed.*, 2014, **53**, 2910.
35. Y. Chen, C. Lu, L. Xu, Y. Ma, W. Hou and J.-J. Zhu, *CrystEngComm.*, 2010, **12**, 3740.
36. L. Mai, F. Yang, Y. Zhao, X. Xu, L. Xu, B. Hu, Y. Luo and H. Liu, *Mate. Today.*, 2011, **14**, 346.
37. Y. Sun, C. J. Takacs, S. R. Cowan, J. H. Seo, X. Gong, A. Roy and A. J. Heeger, *Adv. Mater.*, 2011, **23**, 2226.
38. Z. He, C. Zhong, S. Su, M. Xu, H. Wu and Y. Cao, *Nat. Photon.*, 2012, **6**, 591.
39. X. Chu, S. Liang, W. Sun, W. Zhang, T. Chen and Q. Zhang, *Sens. Actuator B: Chem.*, 2010, **148**, 399.
40. N. Illyaskutty, S. Sreedhar, G. S. Kumar, H. Kohler, M. Schwotzer, C. Natzeck and V. M. Pillai, *Nanoscale*, 2014, **6**, 13882.
41. L. Zheng, Y. Xu, D. Jin and Y. Xie, *Chem. Mater.*, 2009, **21**, 5681.
42. C. Zhu, D. Du, A. Eychmüller and Y. Lin, *Chem. Rev.*, 2015, **115**, 8896.
43. J. Song, X. Ni, L. Gao and H. Zheng, *Mater. Chem. Phys.*, 2007, **102**, 245.
44. J. Song, X. Ni, D. Zhang and H. Zheng, *Solid State Sci.*, 2006, **8**, 1164.
45. G. R. Patzke, A. Michailovski, F. Krumeich, R. Nesper, J.-D. Grunwaldt and A. Baiker, *Chem. Mater.*, 2004, **16**, 1126.
46. W. Pan, R. Tian, H. Jin, Y. Guo, L. Zhang, X. Wu, L. Zhang, Z. Han, G. Liu and J. Li, *Chem. Mater.*, 2010, **22**, 6202.
47. D. Parviz, M. Kazemeini, A. Rashidi and K. J. Jozani, *J. Nanopart. Res.*, 2010, **12**, 1509.
48. W.-S. Kim, H.-C. Kim and S.-H. Hong, *J. Nanopart. Res.*, 2010, **12**, 1889.
49. V. Petrochenkov, I. Gorichev, V. Batrakov, A. Izotov and A. Kutepov, *Theor. Found. Chem. Eng.*, 2004, **38**, 386.
50. A. Chithambararaj, N. Rajeswari Yogamalar and A. C. Bose, *Cryst. Growth Des.*, 2016, **16**, 1984.
51. V. Kumar, X. Wang and P. S. Lee, *Nanoscale*, 2015, **7**, 11777.
52. D. Liu, W. Lei, J. Hao, D. Liu, B. Liu, X. Wang, X. Chen, Q. Cui, G. Zou and J. Liu, *J. Appl. Phys.*, 2009, **105**, 023513.

53.   T. Siciliano, A. Tepore, E. Filippo, G. Micocci and M. Tepore, *Mater. Chem. Phys.*, 2009, **114**, 687.
54.   K. Eda, *J. Solid State Chem.,* 1992, **98**, 350.
55.   W. Dong and B. Dunn, *J. Mater. Chem.*, 1998, **8**, 665.
56.   W. Xu, L. Liu, B. Zhang, Y. Hu and B. Xu, *Ind. Eng. Chem. Res.*, 2016, **55**, 4930.
57.   J. Chang, M. Jin, F. Yao, T. H. Kim, V. T. Le, H. Yue, F. Gunes, B. Li, A. Ghosh and S. Xie, *Adv. Funct. Mater.*, 2013, **23**, 5074.
58.   R. F. de Farias, M. S. Refat and H. A. Hashem, *J Incl Phenom Macrocycl Chem.*, 2008, **61**, 113.
59.   Q. Mahmood, W. S. Kim and H. S. Park, *Nanoscale*, 2012, **4**, 7855.
60.   J. Mendez-Vivar, T. Lopez, A. Campero and C. Sanchez, *Langmuir*, 1991, **7**, 704-708.
61.   F. Bidault, D. Brett, P. Middleton and N. Brandon, *J. Power Sources.,* 2009, **187**, 39.
62.   J. Guo, A. Hsu, D. Chu and R. Chen, *J. Phys. Chem. C.*, 2010, **114**, 4324.
63.   S. Chen and S.-Z. Qiao, *ACS Nano*, 2013, **7**, 10190.
64.   I. V. Lightcap, T. H. Kosel and P. V. Kamat, *Nano Lett.*, 2010, **10**, 577.
65.   D. A. Brownson and C. E. Banks, *Analyst*, 2010, **135**, 2768..
66.   S. Guo and S. Sun, *J. Am. Chem. Soc.*, 2012, **134**, 2492.
67.   S. Stankovich, D. A. Dikin, G. H. Dommett, K. M. Kohlhaas, E. J. Zimney, E. A. Stach, R. D. Piner, S. T. Nguyen and R. S. Ruoff, *Nature*, 2006, **442**, 282.